Deciphering the Influence of Effective Shear Modulus on Neuronal Network Directionality and Growth Cones' Morphology via Laser-Assisted 3D-Printed Nanostructured Arrays

Flamourakis, George; Dong, Qiangrui; Kromm, Dimitri; Teurlings, Selina; van Haren, Jeffrey; Allertz, Tim; Smeenk, Hilde; de Vrij, Femke M.S.; Tas, Roderick P.; Smith, Carlas S.

DOI
10.1002/adfm.202409451

Publication date
2024

Document Version
Final published version

Published in
Advanced Functional Materials

Citation (APA)
Flamourakis, G., Dong, Q., Kromm, D., Teurlings, S., van Haren, J., Allertz, T., Smeenk, H., de Vrij, F. M. S., Tas, R. P., Smith, C. S., Brinks, D., & Accardo, A. (2024). Deciphering the Influence of Effective Shear Modulus on Neuronal Network Directionality and Growth Cones' Morphology via Laser-Assisted 3D-Printed Nanostructured Arrays. *Advanced Functional Materials*, *35 (2025)*(5), Article 2409451. https://doi.org/10.1002/adfm.202409451

Deciphering the Influence of Effective Shear Modulus on Neuronal Network Directionality and Growth Cones' Morphology via Laser-Assisted 3D-Printed Nanostructured Arrays

George Flamourakis, Qiangrui Dong, Dimitri Kromm, Selina Teurlings, Jeffrey van Haren, Tim Allertz, Hilde Smeenk, Femke M. S. de Vrij, Roderick P. Tas, Carlas S. Smith, Daan Brinks,* and Angelo Accardo**

In the present study, the influence of topographic and mechanical cues on neuronal growth cones (NGCs) and network directionality in 3D-engineered cell culture models is explored. Two-photon polymerization (2PP) is employed to fabricate nanopillar arrays featuring tunable effective shear modulus. Large variations in mechanical properties are obtained by altering the aspect ratio of the nanostructures. The nanopillar arrays are seeded with different neuronal cell lines, including neural progenitor cells (NPCs) derived from human induced pluripotent stem cells (iPSCs), I^{3}Neurons, and primary hippocampal neurons. All cell types exhibit preferential orientations according to the nanopillar topology, as shown by neurites creating a high number of oriented orthogonal networks. Furthermore, the differentiation and maturation of NPCs are affected by the topographic and mechanical properties of the nanopillars, as shown by the expression of the mature neuronal marker Synapsin I. Lastly, NGCs are influenced by effective shear modulus in terms of spreading area, and stochastic optical reconstruction microscopy (STORM) is employed to assess the cytoskeleton organization at nanometric resolution. The developed approach, involving laser-assisted 3D microfabrication, neuro-mechanobiology, and super-resolution microscopy, paves the way for prospective comparative studies on the evolution of neuronal networks and NGCs in healthy and diseased (e.g., neurodegenerative) conditions.

1. Introduction

Neurons are highly sensitive to their surrounding mechanical microenvironment.[1] The neuronal growth cone (NGC)[2] is a specialized compartment for axonal outgrowth, driven by cytoskeleton reorganization and dynamics, by which neurons probe the surrounding extracellular matrix to target other cells with the goal of establishing neuronal connections. The study of this specialized sensory structure, rich in microtubules and filamentous actin (F-actin) that drive its growth, is of paramount importance for several applications ranging from fundamental mechanobiology to in vitro disease models and tissue engineering.[3,4] The mechanical properties of the cellular microenvironment of developing neurons can influence the signaling and motility of NGCs.[5] Nonetheless, the evolution of this architecture, whose motility is controlled by specialized actin-rich protrusions (filopodia) and their point contacts (that

---

G. Flamourakis, A. Accardo
Department of Precision and Microsystems Engineering
Faculty of Mechanical Engineering
Delft University of Technology
Mekelweg 2, 2628 CD, Delft, The Netherlands
E-mail: A.Accardo@tudelft.nl

The ORCID identification number(s) for the author(s) of this article can be found under https://doi.org/10.1002/adfm.202409451

DOI: 10.1002/adfm.202409451

Q. Dong, S. Teurlings, D. Brinks
Department of Imaging Physics
Faculty of Applied Sciences
Delft University of Technology
Mekelweg 2, 2628 CD, Delft, The Netherlands
E-mail: d.brinks@tudelft.nl

D. Kromm, C. S. Smith
Delft Center for Systems and Control
Faculty of Mechanical Engineering
Delft University of Technology
Mekelweg 2, 2628 CD, Delft, The Netherlands
E-mail: c.s.smith@tudelft.nl

J. van Haren, T. Allertz
Department of Cell Biology
Erasmus MC University Medical Center
Rotterdam 3015CN, The Netherlands

contain a number of focal adhesion-related molecules[6,7]) has so far been investigated almost exclusively on conventional 2D glass slides,[8] microfluidic biochips,[9] or in the presence of unordered collagen gels.[10] The first two configurations hinder the possibility for the growth cone to probe more biomimetic microenvironments and feature, in the first case, a Young's modulus in the range of $E \approx 70$ GPa, which is much higher than the Young's modulus of the brain tissue ($E \approx 1$ kPa), and in the second approach, the absence of topographic cues. Finally, the third configuration suffers from batch-to-batch variability, typical of collagen and other extracellular matrix-like gels (e.g., Matrigel).[11] Recent studies have highlighted the importance of substrate rigidity and topographical cues in modulating neuronal behavior and function.[12–15] For example, 3D neuronal cultures on soft hydrogel substrates lead to increased neurite outgrowth and branching compared to those on simple 2D stiff substrates.[16–18] Similarly, it was reported that micropillar arrays with specific geometries can guide the alignment and elongation of neuronal processes,[19–22] without anyhow taking into account the role of specific mechanical properties such as the effective shear modulus. This parameter represents the shear modulus sensed by cells when crawling on top of micro- or nano-structures' arrays. By tuning the effective shear modulus of the substrate, changes in mechanical and topographic cues can influence the adhesion, morphology, and phenotype of both stem[23] and primary cells,[24,25] but its relationship with neuronal network directionality and growth cone morphology remains unexplored.

Recent advances in laser-assisted 3D microfabrication techniques, such as two-photon polymerization (2PP), have enabled the design of complex micro- and even nanostructured environment arrays with tunable topographic, optical,[26] and mechanical properties,[27,28] allowing for controlled growth and monitoring of different cell models, including glioblastoma,[29–31] brain microglia,[24] and bone stem cells[28,32] for mechanobiology, in vitro treatment modeling and tissue engineering.[33] In the context of neural tissue engineering, the possibility of tuning the mechanical properties of the biomaterials,[34,35] including polydimethylsiloxane (PDMS)-like elastomers,[36] plays a fundamental role although the capability to manufacture macro-sized specimens[37] must meet a tradeoff with the desired single feature resolution. This level of control has opened new avenues for investigating the role of mechanical and topographic cues in neuronal development, regeneration, and disease modeling. In this study, we report the development and characterization of nanoengineered 3D cell-instructive biomaterials fabricated via 2PP as a reproducible and physiologically relevant platform to unveil the influence of effective shear modulus on the growth of primary and stem-cell-derived neurons. The rationale behind the design of the nanopillars was dictated both by the desired effective shear modulus and by the typical diameter of brain extracellular matrix fibers, which range from tens to hundreds of nanometers in diameter,[38] to influence the behavior of neurites (i.e., dendrites and axons), growth cones, and filopodia (which feature a diameter between 200 and 400 nm[39]). The characterization included morphological and mechanical assessment of the advanced nanostructures as well as morphological and confocal/super-resolution microscopy of neural network orientation and growth cones' development in induced pluripotent stem cell (iPSC)-derived neurons and primary hippocampal neurons. The results showed that across all different neural cell types, cell networks showed different directionality according to the topography and effective shear modulus featured by the specific nanopillar arrays. The effective shear modulus also directly influenced the differentiation of neural progenitor cells (NPCs) and neurites' length. Furthermore, we were able to assess the morphological features (i.e., area and vinculin localization) of 3D neuronal growth cones, both via scanning electron and confocal imaging. Finally, stochastic optical reconstruction microscopy (STORM) was employed for the first time to visualize the interaction between growth cones and 3D-printed biomaterials at nanometric resolution.

2. Results and Discussion

2.1. Design, Fabrication, and Characterization of the Nanopillar Arrays

The nanopillars (**Figure 1A**) were designed to have a diameter of 500 nm and an interpillar gap of 1 µm to enable cells and their neurites to grow on top of them (the typical diameter of a neuronal cell body and of an axon are, respectively, 10–20 µm and 0.1–10 µm[40]) and prevent sedimentation at the bottom of the substrate. We opted for a "strip" design configuration where several arrays of different heights were fabricated next to each other starting with a flat pedestal without pillars, followed by the shortest pillars, and finally ending with the tallest ones (Figure 1B). Concerning the fabrication material, we employed IP-Dip, a photocrosslinkable resin that allows us to reach the highest achievable resolution with our 2PP setup and has already shown to be biocompatible with several cell types[41,42] including neurons.[43] It is important to note how the nanopillars were printed on top of a pedestal made of the same material, IP-Dip, to prevent delamination from the substrate itself. To achieve the "strip" design, an initial small nanopillar array was designed with a size of 120 × 120 µm^2. Then, the small array was replicated n times along the x- and y-axes, leading to a final large array of ≈1 × 1 mm^2. The spacing between different nanopillar arrays was 50 µm, and the overall printing time for each strip was ≈3 h. Moreover, each glass cover slip contained one whole strip. The morphological characterization by scanning electron microscopy (SEM) images revealed that successfully printed pillars had a cylindrical shape with a slightly curved top (Figure 1C,D). This is expected due to the voxel shape (the 3D equivalent of a 2D pixel) of the 780 nm laser femtosecond laser. The voxel geometry is indeed an ellipsoid with an aspect ratio depending on the numerical aperture (NA) of the lens

---

H. Smeenk, F. M. S. de Vrij
Department of Psychiatry
Erasmus MC University Medical Center
Rotterdam 3015CN, The Netherlands
R. P. Tas
Department of BioMechanical Engineering
Faculty of Mechanical Engineering
Delft University of Technology
Mekelweg 2, 2628 CD, Delft, The Netherlands
D. Brinks
Department of Molecular Genetics
Erasmus MC University Medical Center
Rotterdam 3015CN, The Netherlands

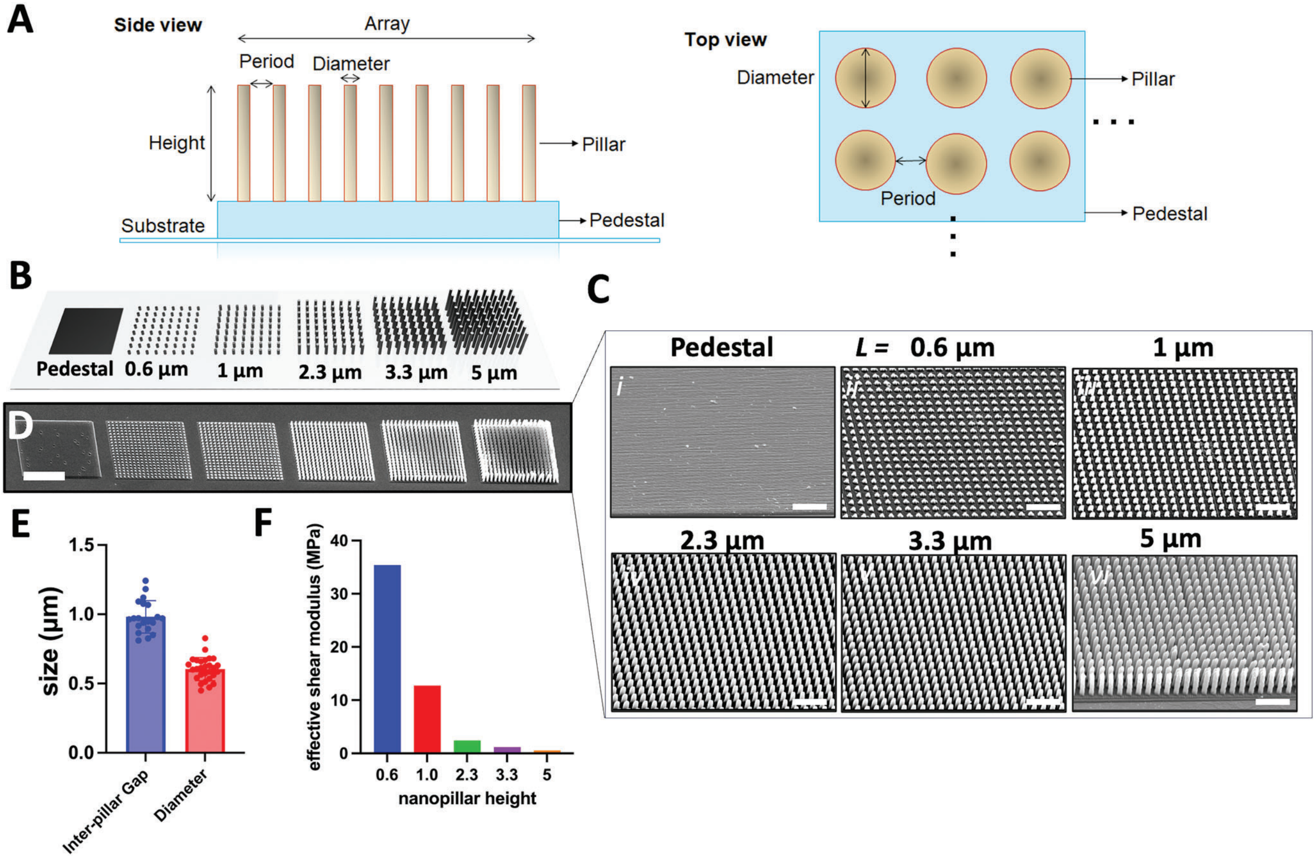

Figure 1. Nanopillar arrays fabrication and characterization. A) Schematic representation of the array parameters. B) 3D rendering of the nanopillars "strip." C) SEM images of the nanopillar arrays with different heights: i) pedestal, ii) 0.6 µm, iii) 1 µm, iv) 2.3 µm, v) 3.3 µm, and vi) 5 µm). Scale bars correspond to 5 µm. D) SEM image of the nanopillars strip (areas of 30 × 30 μm^2 in this picture). Scale bar corresponds to 15 µm. E) Measured interpillar gaps and diameter (in µm). The average and standard deviation are based on $n = 50$ nanopillars measurements. F) Effective shear modulus (in MPa) related to different nanopillars' arrays heights (in µm).

used to focus the laser beam. In our case, we employed a 63× objective lens with NA = 1.4, allowing for a voxel size of lateral diameter (i.e., along the x–y plane) of 200 nm and longitudinal size (i.e., along the z-axis) of 400 nm (ratio 1:2). Different nanopillars' heights were chosen based on the desired effective shear modulus ($\bar{G}$) which can be derived from Equation (1)[23]

$$\bar{G} = \frac{3}{16}\left(\frac{D}{L}\right)^{2} fE \tag{1}$$

where D is the diameter of each pillar, L is the height, f is the surface area covered by pillars per total surface area of the array, and E is the Young's modulus of the polymerized material. L ranged from 0.6 to 1, 2.3, 3.3, and 5 µm. The measured gap between the nanopillars was 1 ± 0.2 µm, allowing the cells and neuritic processes to develop on top of them, while the measured diameter was 0.5 ± 0.2 µm (Figure 1E). We measured the diameter of the pillar and the gap between them at the very top of each pillar, as depicted from the SEM close-up in Figure S1 (Supporting Information). The estimated $\bar{G}$ from Equation (1) spanned ≈2 orders of magnitude from ≈500 kPa up to ≈35 MPa (Figure 1F). To achieve such a wide value span, we tuned the height (L) instead of the gap (and consequently f), as $\bar{G}$ has an inverse quadratic relationship with L, meaning that a small change of L can lead to a significant change of $\bar{G}$. Depending on the fabrication parameters, the Young's modulus of the bulk material can change significantly. To test the tunability of IP-Dip's Young's modulus according to printing parameters, we fabricated several cubes with printing parameters identical to the ones employed for the nanopillar arrays and performed mechanical compression testing. Consequently, we extracted the Young's modulus by calculating the slope of the loading phase of the stress–strain diagram (see Figure S2 in the Supporting Information) and found it to be $E = 2.972 \pm 0.19$ GPa, which is in the same range of the one reported in recent literature.[42,44] Lastly, with this measured value, we could solve Equation (1) to calculate the different $\bar{G}$ for each nanopillar array (Figure 1F). The nanopillar arrays were also mechanically characterized and subjected to compression testing. In Figure S2 (Supporting Information), we report the mechanical stress/strain plots of arrays consisting of 20 × 20 nanopillars (total area 30 × 30 µm).

The arrays with shorter heights, specifically those measuring 0.6 and 1 µm, exhibited no discernible deformation throughout the entire compression cycle as expected. This observation suggests a high degree of structural integrity and resistance to compressive forces within these arrays. Conversely, the arrays with larger heights, namely those measuring 2.3, 3.3, and 5 μm, demonstrated three distinct loading phases. The initial loading phase was characterized by the pillars remaining undeformed up to a strain of ≈ 5%. This phase indicates the inherent strength of the material that enables it to withstand initial compressive forces without any noticeable deformation. Following the initial loading phase, a deformation phase was observed, where the pillars began to deform laterally under the applied load. This deformation was noted to occur within the strain region of 5% to 30%. The onset of deformation indicates the exceeding of the elastic limit of the material, leading to permanent changes in the structure. The final phase, referred to as the "touching" phase, occurred between 30% and 45% strain. During this phase, all pillars came into contact with each other, indicating a significant deformation and displacement of the structures under the applied stress. Additionally, as the pillars become taller, the aspect ratio between height and diameter also increases. We observed that when this ratio reaches 10 (i.e., the nanopillars of 5 μm height and 0.5 μm diameter), some pillars start to touch each other, especially at the edges of the array due to higher capillary forces coming from the solvent evaporation during the chemical development step.[45] The deflected nanopillars account anyhow for <5% of all the nanopillars in the 5 μm array, which is not a major issue for our cell cultures.

By employing the nanopillar arrays as a topographic and mechanical environmental cue, we assessed how neuronal cells interacted with the extracellular scaffold at the cell surface, in terms of network directionality, neuritic length, differentiation, and growth cones morphology. To that end, we employed three different neuronal cell types widely used as models for basic neuromechanobiology[46] and tissue engineering:[1] i) primary hippocampal neurons derived directly from mouse neonatal brain, ii) human neural progenitor cells (NPCs) derived from induced pluripotent stem cells (iPSCs), and iii) human cortical neurons (I^3Neurons, I^3N), obtained by differentiation of I^3N-induced pluripotent stem cells.[47,48] Depending on the maturation level of each cell line, the cells were left in cell culture for different time periods. Hippocampal neurons were cultured for 14 days in vitro (DIV); NPCs were monitored at a 6 week differentiation time point; finally, I^3N cells were characterized after a maturation period of 1 week. The neuronal morphology and network formation of all cell lines on the nanopillars were qualitatively and quantitatively investigated using SEM and immunofluorescence microscopy, while the NGCs of I^3Neurons were assessed by SEM, confocal microscopy, and super-resolution microscopy.

2.2. Characterization of Primary Hippocampal Neurons on the Nanopillars Arrays

Figure 2A–D depicts the behavior of primary hippocampal neurons on the different nanopillar topographies for which cells display remarkable changes in terms of morphology. Notably, cells align along the pillars, exhibiting a directional preference. The height of nanopillars is crucial, as heights exceeding 1 μm enhance directional responsiveness, as shown in Figure 2B–D.

As cells traverse the pillar-studded terrain, their somas (cell bodies) and neuritic processes (such as dendrites and axons) exhibit distinct behavior. These cellular components predominantly reside atop the pillars without making contact with the substrate beneath (Figure 2A). Due to the small inter-pillar gap (<1 μm), the cell somas were indeed localized on top of all nanopillar arrays instead of adhering on their sidewalls or sedimenting at the bottom of the substrate. Surprisingly, the neurites also feature a predisposition to develop on the top of each pillar, even if their diameter was much smaller than the 1 μm interpillar gap.

A more detailed overview of the neuronal networks is reported in the confocal microscopy images of Figure 2B. Here, we stained for different compartments of the cells: nuclei (DAPI, cyan), F-Actin (cytoskeleton, red), and β-tubulin III (early maturation neuronal marker, green). To extract the neurites' directionality, the green channel was employed (Figure 2C; Figure S3, Supporting Information). The neurites follow the nanopillars' topology. More precisely, we observe that the cells follow the directionality of the pillars' lattice, which is either 0° or 90°. The measured orientations are depicted in Figure 2D. We assumed the 0° orientation along the x-axis and the + or −90° along the y-axis in relation to the pillar lattice (Figure 2E).

Consequently, a neurite would have a 0° orientation when developing along the x-axis and a 90° when developing along the y-axis. As we can see from the directionality diagrams reported in Figure 2D, the largest amount of the measured neurites is sharply aligned onto the nanopillars along + or -90° orientation. Especially for the highest pillar array, the orientation peak is also observed at 0°, allowing neurites to intertwine in a cross pattern resembling the directionality featured by hippocampal neurons in their native tissue environment.[49] This orientation effect is lost in presence of 0.6 μm height arrays, and the neurons' phenotype remains the same as the one observed on the flat IP-Dip pedestal and the glass control where neurites develop in a random way due to the low nanopillar arrays aspect ratio. Also, we observed that the histogram peaks are less prominent the shorter the pillars are. These results suggest that the height, and more precisely, the effective shear modulus, plays an important role in the orientation of the neurites. We attribute this to the fact that the diameter of the neurite is small enough to be confined between two pillars (refer to Section 2.4.1 for a similar behavior observed in I^3 neurons), thus forcing it to grow in line with their orientation.

2.3. Characterization of iPSC-Derived NPCs on the Nanopillars Arrays

2.3.1. iPSC-Derived NPCs' Differentiation and Orientation Are Affected by the Nanopillars

One of the most widely employed cell types in neuroscientific research are NPCs derived from human iPSCs.[50] Upon differentiation, these cells exhibit phenotypic characteristics akin to primary neuronal cell lines, such as primary hippocampal or cortex neurons. The cells were seeded onto the nanopillars in their neural progenitor state and allowed to differentiate over a period of 6 weeks prior to analysis. **Figure 3** provides a visual representation of the behavior of NPC-derived neural networks following a 6 week differentiation period at an initial seeding of 50 000 cells/well. The directionality of the

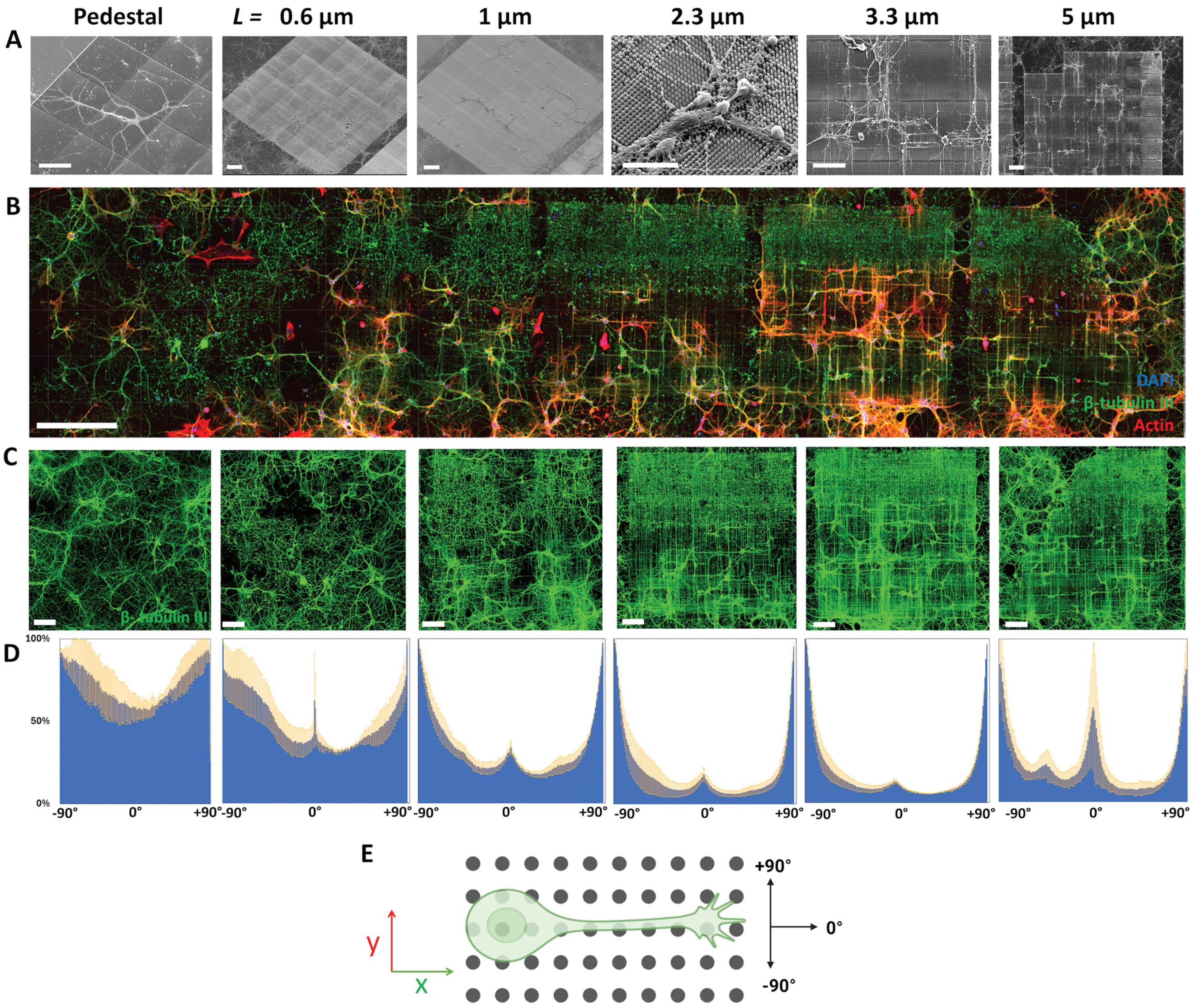

Figure 2. Hippocampal neurons after 14 DIV on the nanopillar arrays strip. A) SEM images of the pedestal and different heights of nanopillar arrays from 0.6 to 5 µm. Scale bars correspond to 50 µm. B) Confocal images of the pedestal and the nanopillar arrays. Green: β-tubulin III, red: F-Actin, cyan: DAPI. Scale bar corresponds to 100 µm. C) Representative confocal images employed for neurites; directionality (green: β-tubulin III). Scale bars correspond to 50 µm. D) Orientation plots of neurites for each nanopillar array. Yellow standard deviation error bars correspond to the average orientations of $n = 3$ experiments. The y-axis has normalized values to the highest value of the orientation histogram generated for each array. E) Graphical representation of a neuron on the nanopillars and the corresponding angular orientations.

neurites on the different nanopillar arrays was analyzed using confocal microscopy. As observed previously for hippocampal neurons in Figure 2, the dendrites exhibited directionality at 90° and 0°, corresponding to the orientation of the pillars (Figure 3A,B). As shown also for primary neurons, this effect was not observed in presence of 0.6 µm tall nanopillar arrays and on the flat substrates. Given that this cell line differentiates directly on the nanopillars and is not seeded already at its mature stage like in primary hippocampal neurons, it was imperative to confirm that the cells analyzed were indeed featuring mature neuron features. To verify that NPCs differentiated to neurons on the nanopillar and flat substrates, we performed immunolabeling experiments to test for the expression of mature neuronal markers. The cells were thus stained for Synapsin I, a presynaptic neuronal functional marker (Figure 3C).

Interestingly, the intensity of the staining was, on average, substantially higher for neurons on the nanopillar arrays compared to those on the flat control, an observation suggesting that cells on the nanopillar arrays express a higher number of pre-synaptic areas compared to the control, leading to potentially higher amount of synapses forming between the different neurons. We attribute this enhanced expression to the increased directionality of the dendrites on the nanopillar arrays, which may induce the formation of synapses between different cells, thereby enhancing their differentiation.[51] Due to the late time point at which the cells were fixed, it was not possible to assess the morphology of growth cones on the pillars.

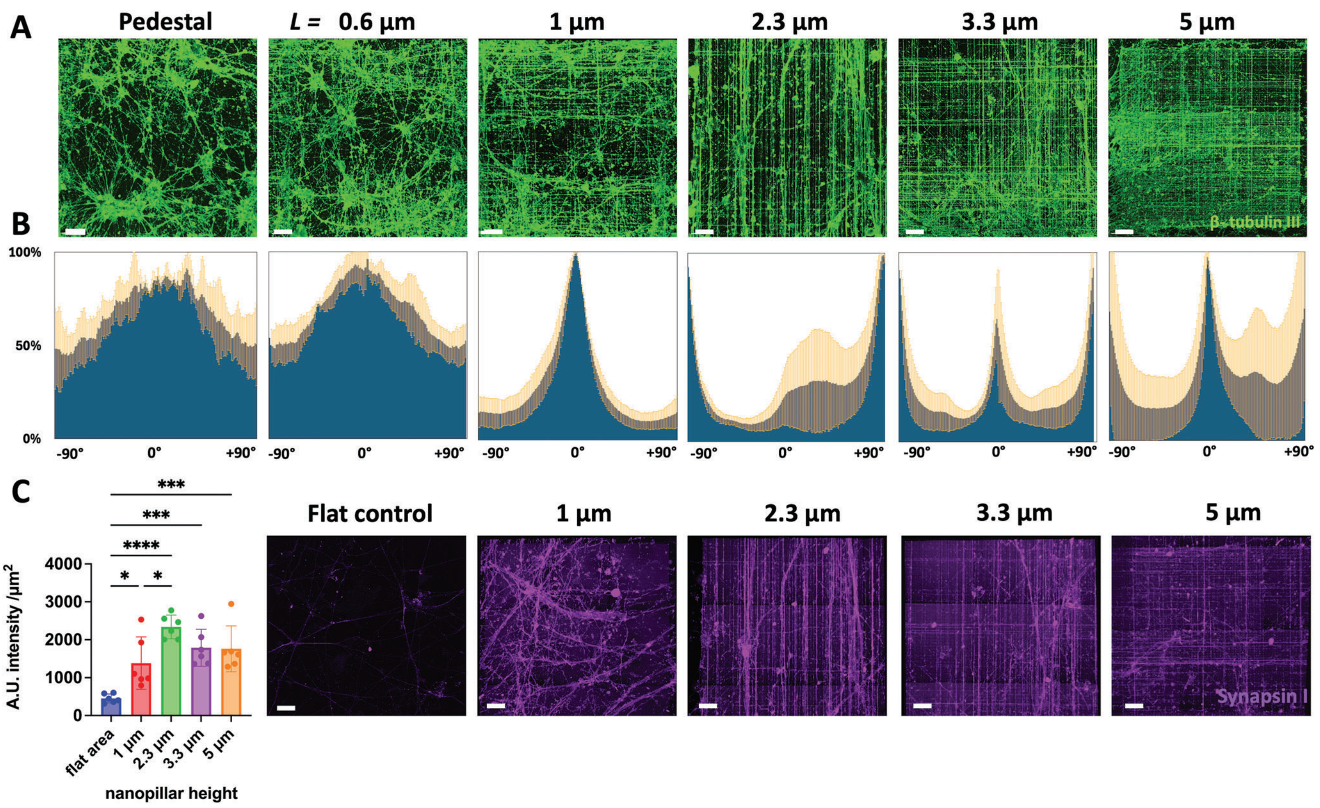

Figure 3. NPCs seeded and differentiated on different height nanopillar arrays. A) Confocal images of neural networks after 6 weeks of differentiation on the pillars. Green: β-tubulin III. Scale bars correspond to 30 µm. B) Orientation histogram plots (blue) reveal the directionality of dendrites to be either 90° or 0° on the nanopillars compared to the flat control. The standard deviation (yellow) for each bar was calculated from $n = 3$ samples. C) Synapsin I staining confocal images reveal that the expression of Synapsin I is higher in the presence of the nanopillars compared to the flat control. Scale bars correspond to 30 µm. For the statistical analysis, images were acquired and analyzed for neurite Synapsin I intensity normalized to the total neuritic area ($n = 5$). A one-way analysis of variance (ANOVA) test and a Tukey test were conducted to evaluate the p-values of the different groups. Statistically significant results were considered to have $p < 0.05$ and were annotated with asterisks. p-values = $^*p < 0.05$, $^{**}\,p < 0.01$, $^{***}\,p < 0.001$, and $^{****}\,p < 0.0001$.

This is due to the high cell density and because axons are capable of progressing at a relatively high speed (8 µm h^{-1})[52] surpassing the total area of the pillar and propagating to the glass substrate.

2.3.2. Nanopillar Arrays Induce the Formation of NPCs' Neurospheres

When NPCs are seeded on the nanopillars at a lower density (10 000 cells/well), they initiate the formation of so-called neurospheres.[53] The process begins with cell proliferation, followed by cell migration and aggregation. Subsequently, the aggregated cells create a large spherical structure called a neurosphere. **Figure** 4A illustrates the behavior of NPCs on the strip after 6 weeks of differentiation.

We systematically ($n = 10$) observed the formation of a single neurosphere on the tallest nanopillar array, which is the one featuring the lowest effective shear modulus (0.5 MPa). Several neurites sprouted as large bundles from the neurosphere, extending toward both the other arrays and the glass substrate. After extending over ≈300 µm, these bundles disentangled into individual neurites that connected to each other, creating complex networks. The networks are also directional, following the nanopillar arrays underneath (Figure 4B). As revealed by SEM images (Figure 4C), neurites were found to remain on top of the pillars, further contributing to the complexity of these networks. Also, the neurites on the pedestal and on the glass substrates look very flat and form scant networks (Figure 4B), whereas, on the pillars, they keep their cylindrical shape and feature multiple connections with neighboring cells. Neurites expressing both F-Actin and β-tubulin III have the ability to adhere to the extracellular matrix (ECM) using point contact adhesions.[6] When provided with a flat surface, there is a higher number of point contact adhesions all around the neurites, thus increasing the tension that neural filopodia experience.[54] Especially when the substrate features high Young's modulus, the tension becomes higher, allowing for a spread phenotype. On the other hand, nanopillars limit the number of anchoring points a neurite has (like with the fibers of the natural brain ECM), inducing the development of fewer point contact adhesions and, ultimately, allowing for a more cylindrical neuritic conformation.

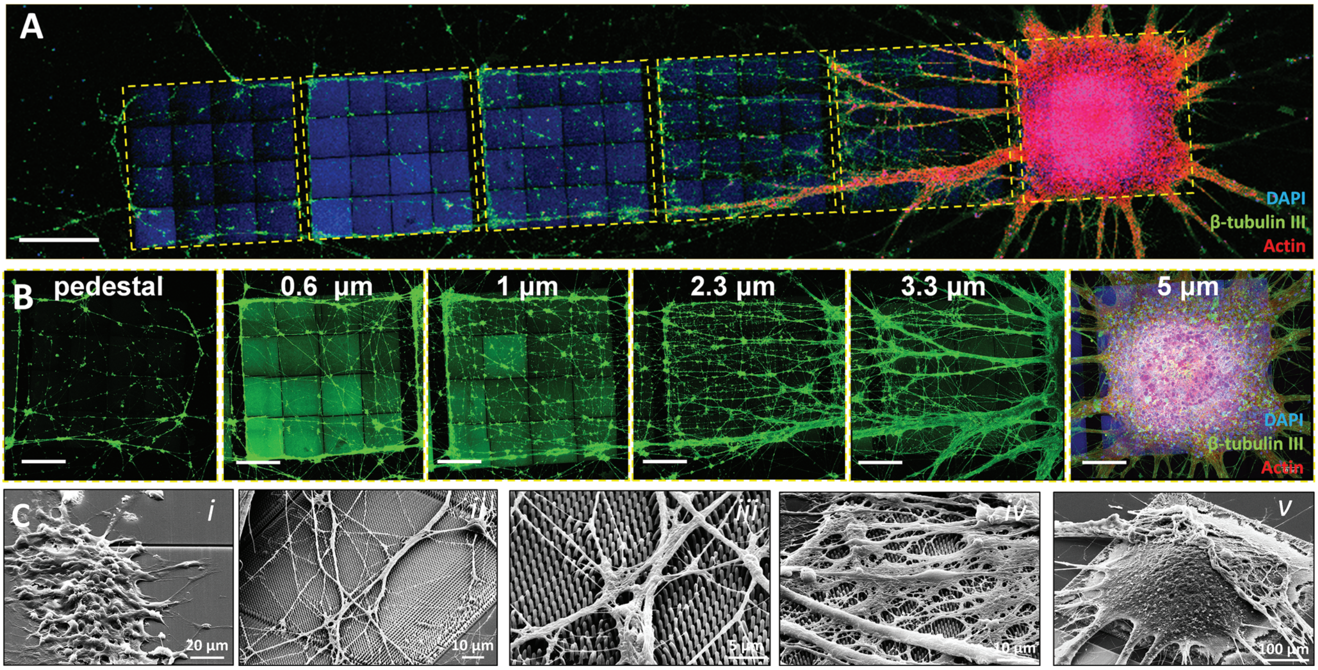

Figure 4. NPCs were seeded directly on nanopillar arrays. A) Confocal mosaic image of the whole nanopillars strip and pedestal with NPCs' neurosphere formed onto the tallest nanopillar array (5 µm). Scale bar corresponds to 300 µm. Green: β-tubulin III, red: F-Actin, and cyan: DAPI. B) Confocal images of individual arrays with dendrites stained for β-tubulin III. Scale bars correspond to 120 µm. C) Representative SEM images of the cells on the pillars: i) pedestal, ii) 2.3 µm, iii), iv) 3.3 µm, and v) 5 µm.

2.4. Characterization of I^{3}Neurons on the Nanopillars' Arrays

2.4.1. I^{3}N Cells' Characterization and Growth Cone Morphology

The third cell line we employed was I^{3}Neurons. This cell line is derived from human iPSCs that can be induced to rapidly differentiate into mature functional neurons in a very short period of time.[48] After 1 week of culture, cells were fixed, stained for β-tubulin III, and observed under the confocal microscope (**Figure** 5A). A similar behavior compared to the other two cell lines before was observed with neurites' orientation influenced by the nanopillar arrays. Directionality histograms show distinctive peaks at 90° and 0° for all arrays, an effect that is lost in presence of flat controls (Figure 5B), agreeing with the obtained previous results. The directionality histograms for this cell type also include peaks at 45°. Taking into consideration the nanopillar configuration, 45° corresponds to the distance between the diagonals of two pillars (for the orthogonal distribution of pillars and a gap of 1 µm, this distance is ≈1.4 µm).

The speed at which these cells differentiate into neurons can play a key role in this context. Given the forced neuronal differentiation through neurogenin-2 (Ngn2) overexpression in this cell line[48] (see the "Experimental Section"), I^{3}Neurons' neurites can reach longer lengths at much earlier time points compared to conventional NPC-derived neurons. Considering their exploratory nature, neurites could indeed sprout from the cell soma and remain between the diagonal of the nanopillars, a behavior not observed in the slower maturing neural networks derived from NPCs.

Concerning NGC morphology, after only 1 week of maturation, I^{3}Neurons enabled straightforward detection of NGCs (Figure 5C,D). As depicted in the confocal images (Figure 5D), NGCs are identified by neurites (expressing β-tubulin III, green) ending in lamellipodia, large areas of a quasi-2D F-Actin mesh (red), with several filopodia sprouting outward to probe the surrounding environment. This conformation changes in the presence of nanopillars higher than 1 µm, where the NGCs are characterized by smaller lamellipodia areas, while the filopodia reach areas distant several micrometers from the main NGC region. To quantify the influence of effective shear modulus, the NGC area was measured from the end of the axon shaft where the transition zone begins until the end of the filopodia (i.e., the overall NGC area is the sum of both filopodia and lamellipodia). NGCs on flat stiff surfaces (glass and IP-Dip pedestals) remained spread and had a significantly larger area than NGCs growing on the nanopillar arrays except the 0.6 µm one (Figure 5C,D). More precisely, NGCs on flat surfaces were ≈60% larger than the ones on the 0.6 µm high nanopillar arrays ($\bar{G}$ = 35 MPa) and ≈ 4-fold larger than the NGCs on the 3.3 µm ($\bar{G}$ = 1.17 MPa) and 5 µm ($\bar{G}$ = 500 kPa) high ones. Therefore, it is clear how effective shear modulus has a significant effect on the development and morphology of NGCs as phenotypically, the shape differs substantially. This difference is supported by the fact that previous in vivo experiments suggested that NGCs create long protrusions and feature a narrow morphology, as the natural ECM in the brain can guide axonal outgrowth.[55]

The detailed localization of neurites and NGCs was investigated also by scanning electron microscopy. **Figure 6** depicts SEM images of the nanopillar arrays colonized by I^{3}Neurons. All cell

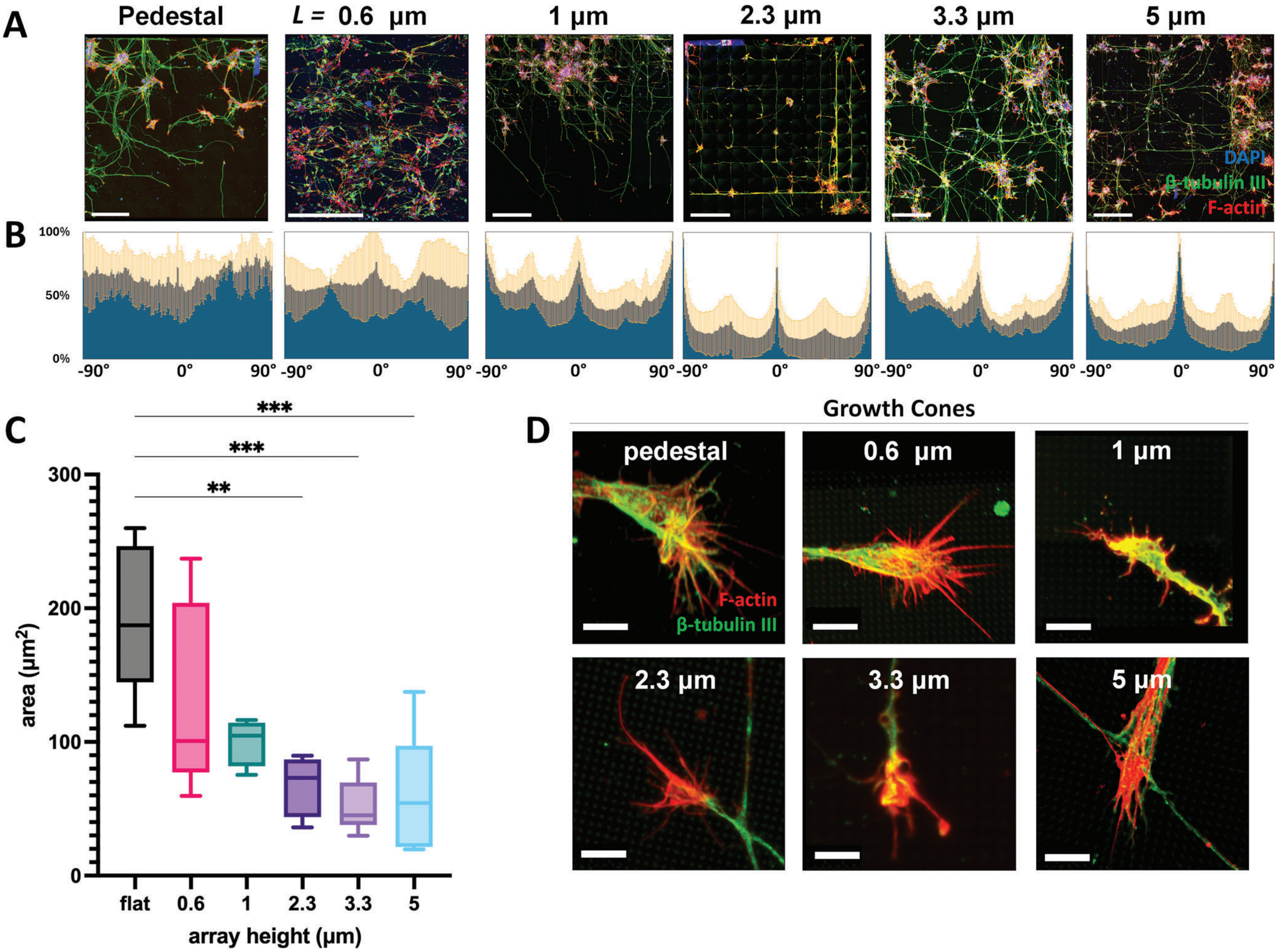

Figure 5. I^{3}Neurons culture on the nanopillars arrays. A) confocal image of the cells on the arrays and the pedestal. Green: β-tubulin III, red: F-Actin, cyan: DAPI. Scale bars correspond to 50 µm. B) Orientation histograms corresponding to the neurites of the cells on each array ($n = 3$). C) Plot of the area of NGCs on different nanopillar arrays. Ten NGCs were measured from each condition ($n = 5$). One-way ANOVA with Tukey test was conducted to calculate the p-values. Statistically significant results were assumed to have $p < 0.05$. p-values: $^{*}p < 0.05$, $^{**}p < 0.005$, and $^{***}p < 0.001$. D) Representative confocal images of NGCs on different nanopillar arrays. Red: F-Actin, green: β-tubulin III. Scale bars correspond to 10 µm.

somas were found to be positioned on top of the pillar arrays, thus not infiltrating between them or at the bottom. Neurites exhibited a similar behavior. More precisely, we observed that for nanopillar heights of 1–5 µm, neurites predominantly resided on the upper segment of the pillar (Figure 6A,B). On the other hand, an interesting phenomenon occurred in presence of the 0.6 µm height array (Figure 6C). Due to the shorter height of the pillar, cells and neurites made direct contact with the substrate. As a result, the height effect was lost, potentially explaining the loss of neuronal directionality observed on this specific array.

An intriguing aspect emerged when studying growth cones. These structures, responsible for axon elongation and guidance, exhibited peculiar behaviors in the presence of different nanopillar arrays. As previously mentioned, growth cones include extremely thin protrusions called filopodia (with a diameter of a few hundred nanometers). While the main body of the growth cone remained on top of the nanopillars, filopodia explored the full depth, occasionally reaching down to the flat surface (Figure 6D). The nanopillar arrays allowed, therefore, the growth cone to develop and move along the three axes, which further explains the completely different morphology compared to spread growth cones growing on 2D stiff bulk surfaces (Figure 6E). The effective stiffness that cells and their neurites experience while interacting with the nanopillars depends on the architectural features of the biomaterial and is significantly softer than the stiffness of the material that the microstructures are composed of, as reported for other microstructures interacting with mesenchymal stromal cells.[56] This means that the nanopillars can deform more easily (therefore opposing a hypothetically softer material than bulk) under the forces exerted by one or more cells, compared to bulk surfaces. For small strains (where our nanopillars remain undeformed, as reported in Figure S2B in the Supporting Information), the flexural modulus,[57] which is typically measured for beams made of isotropic material and constrained at both ends by fixed supports (unlike our nanopillars), is equivalent to the Young's modulus. The effective shear modulus, which in previous studies[23] influenced the differentiation of human

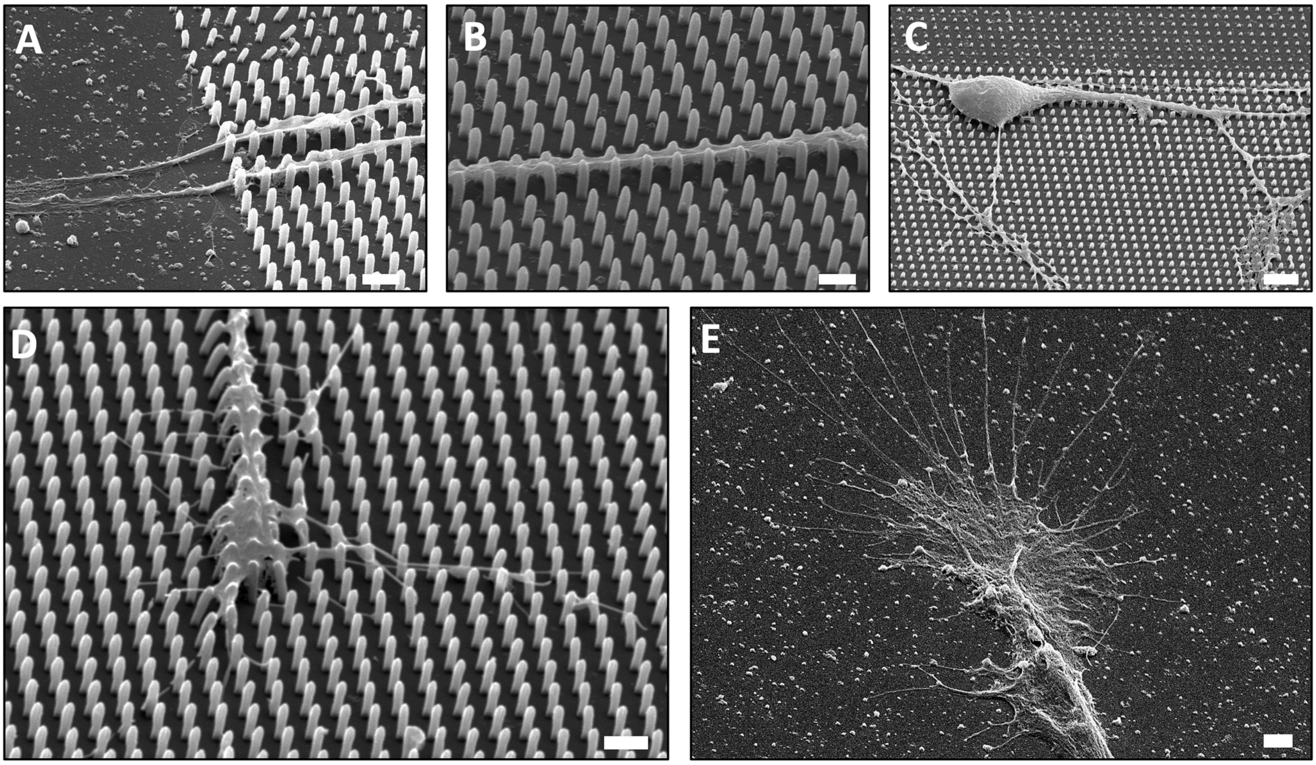

Figure 6. SEM images of I^{3}N cells after 2 weeks of culturing on nanopillars. A) SEM image of dendrites migrating from the glass substrate to the 3.3 µm array. B) Image of a neurite on the nanopillars, where it propagates in the space between the pillars and not on top of them. C) SEM image of an individual cell on the 0.6 µm array. D) Growth cone on 3.3 µm array. E) Growth cone on a glass substrate. Scale bars correspond to 2 µm.

embryonic stem cells toward pancreatic endoderm cells, is therefore a more relevant parameter for our model.

2.4.2. Neurite Length Is Affected by the Nanopillar Arrays

When neurons are seeded on different substrates, after an initial attachment phase, they start to develop protrusions, known as neurites, growing from their somas. Environmental cues are known to guide neurites along the path to axonal fate, dendrites or dendritic trees.[58] The mechanical properties of the substrate that a neurite innervates can significantly affect the way it extends.[8] We hypothesize that when tailored extracellular cues are provided, neurites are able to develop complex networks and longer lengths than those on conventional substrates (i.e., stiff, flat substrates). To evaluate the influence of the effective shear modulus of the nanopillar arrays on neurite length, we used I^{3}Neurons cultured on the arrays for 2 days. The results are summarized in **Figure** 7A,B.

Neurons that are cultured on the flat surface feature the shortest neurites with the longest one not exceeding 166 µm. The cells that were seeded on the nanopillars, appeared to have significantly longer neurites, with a peak of 430 µm length on the 2.3 µm height array. Lastly, neurites on 3.3 and 5 µm arrays seemed to be shorter in lengths compared to the 2.3 µm array, which we attribute to the fact that NGC on those arrays displays a 3D phenotype due to the high aspect ratio of the nanopillars (Figure S4, Supporting Information). This configuration can slow down the NGC's exploration of the surrounding 3D environment, as it takes significantly more time for the filopodia to probe space along three axes (x, y, z) instead of two (x, y), and steer the direction of the axonal outgrowth. We speculate that this could be one of the mechanical cues and underlying causes influencing specific neural morphology in different regions and layers of the brain. Nonetheless, disentangling these stimuli would require dedicated in vivo experiments (e.g., Zebra fish[55]) where NGCs are imaged in their native environment.

2.4.3. Vinculin Localization in the NGC Is Affected by the Nanopillar Arrays

Vinculin is a very important component of the mechanotransduction pathway as it is one of the primary components of point contact adhesions,[6,59] a complex of proteins that is responsible for cell–matrix and cell–cell adhesion. It was previously shown that vinculin is a key factor for neuronal mechanosensing,[60] suggesting that it acts as a key mechanosensor involved in the regulation of growth cone motility. To that end, we tried to decipher how vinculin interacts with the nanopillar arrays and how the shape of NGCs is affected by the specific localization of vinculin. **Figure** 8 shows confocal images of NGCs of I^{3}Neurons after 2 days in culture, where each row represents the different nanopillar arrays' height.

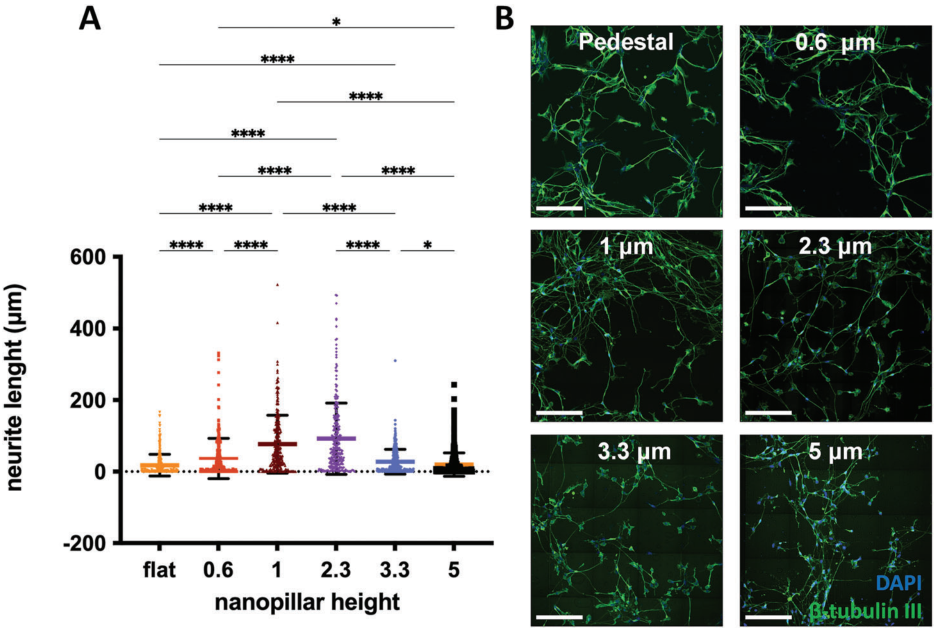

Figure 7. Neurite length analysis of I^{3}Neurons after 2 days in culture. A) Scatter plot of neurites lengths on different nanopillar arrays. Number of neurites measured across a sample size of $n = 3$ samples (flat substrates: 346 neurites; 0.6 µm nanopillar height: 231 neurites; 1 µm: 245 neurites; 2.3 µm: 254 neurites; 3.3 µm: 282 neurites; and 5 µm: 318 neurites). One-way ANOVA with Tukey test was conducted to calculate the p-values. Statistically significant results were assumed to have $p < 0.05$. p-values: $^{*}p < 0.05$, $^{**}p < 0.005$, $^{***}p < 0.001$, and $^{****}p < 0.0001$. B) confocal images of I^{3}Neurons on different nanopillar arrays. Cyan channel: DAPI; green channel: β-tubulin III. Scale bars correspond to 100 µm.

An early cell culture time point is crucial as the neurites, after some days, become too long to enable the identification of growth cones. On the 0.6 µm height nanopillars arrays and flat controls, a higher concentration of vinculin staining is observed in the lamellipodia areas. For these two configurations, the filopodia are (qualitatively) shorter, and the NGC is overall spread, as shown also by the NGC area analysis (Figure 5C). Moving to higher nanopillar arrays (over 1 µm), the vinculin starts to be observed in the filopodia as well as in the lamellipodia, where the concentration is higher than in the filopodia. Moreover, the presence of vinculin is accentuated in the neurites featuring the presence of NGCs. This observation is attributed to the fact that lamellipodia constitute the most stable region of the NGC, which needs to anchor at the ECM and let the filopodia free to probe the surrounding environment. The lack of vinculin, on the other hand, confers a much higher degree of freedom to the filopodia to dynamically elongate and retract when they examine the surrounding environment. When nanopillars are present, the vinculin in filopodia is localized only in proximity to the pillars as that is the only structure they can adhere to (Figure S5, Supporting Information). Moreover, the larger NGC area on flat surfaces and short nanopillars arrays that was observed in Section 2.4.1 could also be attributed to the higher localization of vinculin, as more point contact adhesions can enable a stronger adhesion and, consequently, a more spread morphology.

2.4.4. *Super-Resolution Microscopy of the Growth Cones*

NGCs, in general, are characterized by nanometric features, and they include mainly F-Actin and microtubules that are directly involved in cell crawling. Due to their small diameter, F-Actin and microtubules (≈ 7 and 25 nm, respectively) are difficult to resolve by conventional confocal microscopy. To be able to resolve these structures at a resolution below the diffraction limit, we employed STORM with a refractive index matched imaging buffer,[61] and the results are summarized in **Figure 9**. The experimental setup is described in Figure S6 (Supporting Information). With this technique, we were able to resolve both F-Actin (blinking obtained with phalloidin Alexa Fluor 647) and microtubules (blinking obtained with Alexa Fluor 488) in the same imaging buffer, which provided similar kinetics and fluorophore blinking for both colors. On glass, microtubules form continuous filaments (Figure 9A) that span from the axonal shaft all the way to the transitional zone of the growth cone, where they stop being organized as bundled filaments but become more disentangled and mainly localize at the lamellipodium. Moreover, filopodia feature relatively thick F-Actin filament structures at the peripheral area of NGC (Figure 9B).

In the presence of nanopillar arrays (Figure 9C), we show a qualitative indication of how β-III tubulin bundles are much thinner than on flat control and adhere to the sides of the nanopillars, confirming the results obtained earlier (Figure 5C,D), where NGCs feature smaller areas on nanopillar arrays. Due to the high laser power employed to transition the fluorophores from their dark state and achieve the blinking process, nanopillar arrays higher than 1 µm could not be characterized due to their high intrinsic autofluorescence background, thus not enabling the super-resolution image reconstruction. In future work, we will develop effective biomaterial autofluorescence suppression protocols to enable the super-resolution imaging also of higher aspect ratio nanostructures.

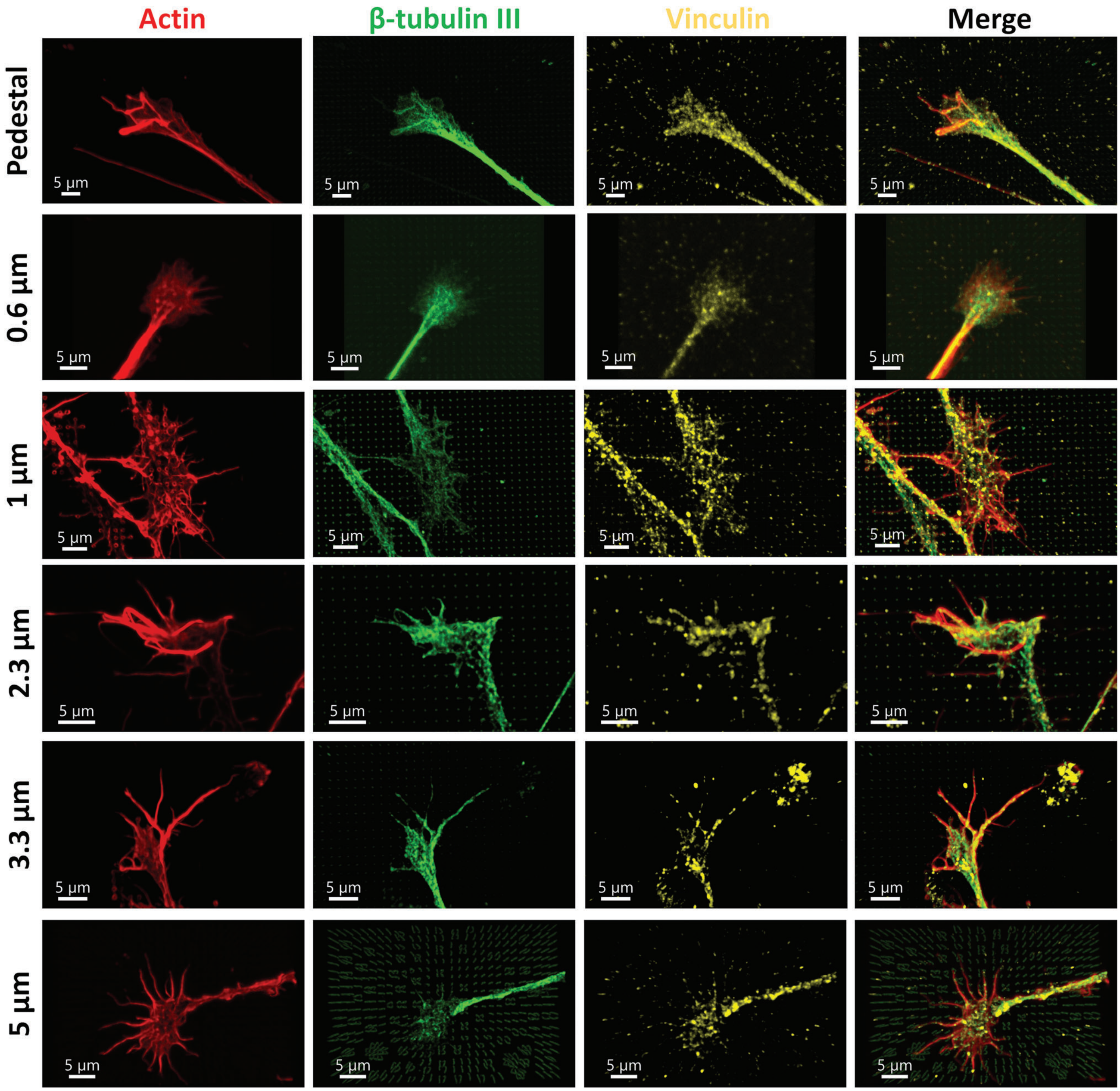

Figure 8. I^{3}Neurons' growth cones on different nanopillar arrays. Red: F-actin, green: β-tubulin III, and yellow: vinculin.

2.5. Overall Comparison of the Nanopillar–Cells Interaction across the Three Cell Models

In this study, we employed three distinct neuronal cell types to examine their behavior when cultured on nanopillar arrays of varying heights. First, hippocampal neurons were isolated from mouse pups and directly seeded onto the nanopillars. SEM and confocal microscopy revealed that these neurons exhibited preferential neurite alignment along the nanopillar configurations (Figure 2).

Next, NPCs were seeded at both high (50 000 cells mL^{-1}) and low (10 000 cells mL^{-1}) densities on the nanopillars and allowed to differentiate into neurons over 6 weeks. In high-density cultures, neurites displayed directional guidance similar to that of hippocampal neurons. Furthermore, to assess the maturation level of these cells differentiated on the nanopillars, we monitored Synapsin I expression, and observed that cells on the nanopillar arrays express a higher number of pre-synaptic areas compared to the control. In low-density cultures, cells formed neurospheres exclusively on the tallest nanopillar arrays (5 µm), which had the lowest effective shear modulus, with axons extending outward.

Lastly, we investigated I^{3}Neurons, which were seeded on the nanopillars due to their rapid differentiation into neurons,

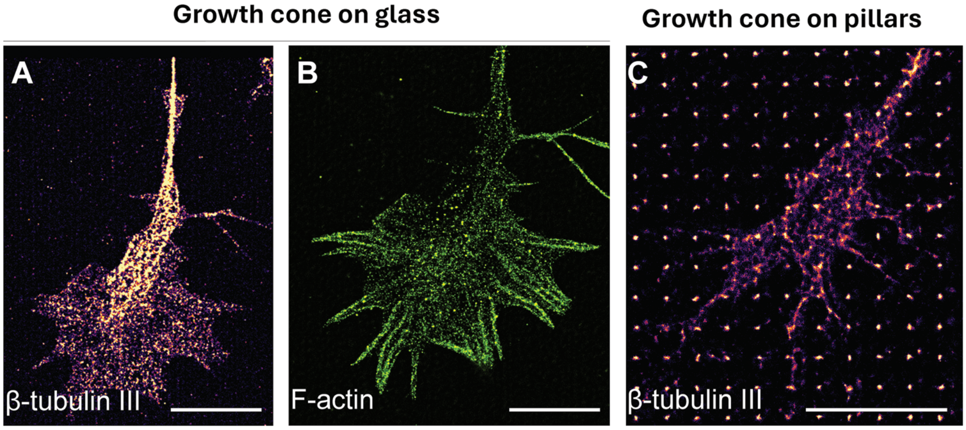

Figure 9. Super-resolution microscopy of I^{3}Neurons NGCs on flat surface and 1 µm height nanopillar arrays. A) Microtubules on glass. B) F-Actin on glass. C) Microtubules on nanopillars. Scale bars correspond to 5 µm.

making them suitable for detailed analysis of growth cone morphology and neurite lengths. The results demonstrated that different nanopillar heights significantly influenced growth cone morphology, area, and vinculin concentration as well as neurite lengths. Their directionality was also affected by the nanopillar configuration, as shown in the other two cell types.

3. Conclusions

Over the past decade, there has been a great effort to create biomimetic environments for a plethora of neuronal cell lines for investigating the mechanobiology behind neuronal networks directionality and growth cones development. In the present study, we 3D-printed nanometric pillar arrays using two-photon polymerization and seeded them with three distinctive neuronal cell lines, derived from human pluripotent stem cells and mouse primary hippocampal neurons. By tuning the aspect ratio of the nanopillars, a range of effective shear moduli from the kPa to the MPa range were achieved, which ultimately influenced the way neurons perceive their extracellular environment. The wide variety of cell lines enabled a comparative assessment of cell responses in terms of morphology, directionality, differentiation, and growth cone development. We demonstrated that all three cell types follow an overall similar trend over the nanopillar arrays. More precisely, arrays with heights of more than 1 µm fostered cell orientation along the lattice of the nanopillars, thus enabling the development of neuronal networks of either 90° or 0°. Such orientations are important in developmental biology, as axons must be able to find their way through the ECM to make synapses with other neurons. Moreover, neurons feature distinctive orientations in-vivo, as shown, for example, in the native environment of mouse hippocampus, where the soma remains at the outer shell and the axons are protruding inward along the same direction,[49] and in the human cortex.[62] The expression of Synapsin I, a mature neuronal marker, of NPCs was significantly higher compared to the flat surface control. By fostering the differentiation of NPCs, we conclude that the combined action of nanopillar topography (resembling the diameter of brain ECM fibers),[38] lattice configuration, and low effective shear moduli create an ideal environment for neurons to be cultured.

We also deciphered the morphology of NGCs of I^{3}Neurons in terms of shape, size, and point contact adhesions' localization. We first analyzed the size of growth cones using confocal microscopy and showed that, on stiff and flat substrates, the area of the growth cone is significantly larger on flat surfaces than the one on tall nanopillar arrays, a fact that is attributed mainly to larger lamellipodia due to the bulky flat surface beneath them. We also observed that the NGCs' filopodia on the nanopillars are much longer than those on flat surfaces (thus further enabling the intrinsic exploratory nature of the NGC) and that they are able to probe the surrounding environment along x-, y-, and z-axes instead of 2D like on the flat control. This is attributed to the fact that the nanopillars, which attempt to mimic the brain ECM fibers diameter, provide biomechanical constraints to the NGCs. The presence of nanopillar arrays also influenced the I^{3}Neurons' neurites lengths, making them significantly longer than those growing on the flat control due to a better representation of the in vivo conditions. Finally, concerning vinculin localization, we showed that point contact adhesions are created only around the nanopillars. In summary, for the first time, we were able to combine laser-assisted 3D printing, mechanical engineering, and super-resolution microscopy to unveil the effect of nano-topographic and mechanical cues on the neuro-mechanobiology of both primary and stem-cell-derived neuronal networks, specifically in terms of neurites directionality and growth cone morphology. Our engineered 3D nanostructures featuring brain ECM fibers like topography and mechanical properties provide, therefore, a novel, physiologically relevant, and reproducible 3D in vitro model to investigate fundamental neuro-mechanobiology mechanisms and, in the future, to assess the development of neuronal networks and growth cones in diseased conditions.

4. Experimental Section

Two-Photon Polymerization Setup Configuration: A commercial 2PP setup (specifically, the Photonic Professional GT+, Nanoscribe GmbH and Co. KG) was employed for fabricating both 2D pedestals and 3D nanopillar array scaffolds. The design of the 3D structures was developed by using Computer-Aided Design (CAD) software, specifically Fusion 360 (Autodesk Inc.). After designing, the scaffold models were exported in STL format. Subsequently, the Nanoscribe DeScribe software was employed to elaborate the STL file, converting it into Nanoscribe's General Writing Language (GWL). Finally, the GWL file was provided to the NanoWrite program, which controlled the 2PP setup. During the conversion process, the STL file was sliced into 2D layers, and each of these layers was then transformed into a set of hatched lines. To create the structures, a droplet of photo-crosslinkable acrylate negative-tone polymer, known as IP-Dip, was cast onto a cleaned and silanized fused silica cover slip (with a thickness of 300 μm and a diameter of 13 mm). The substrates were cleaned and activated using O_2 plasma (generated by a Femto plasma etcher, Diener) at a power of 100 W for 40 min, with an O_2 flow rate of 5 sccm and a pressure of 0.16 bar. Afterward, the substrates were silanized overnight using pure 3-(trimethoxysilyl) propyl methacrylate (MAPTMS) from Sigma–Aldrich, followed by rinsing with isopropanol and drying with compressed air. Silanization enhances the adhesion of the photosensitive biomaterial to the substrate. The next step involved exposing the resin to a 780 nm wavelength femtosecond pulsed laser (with a power of 37.5 mW, corresponding to 75% power and 2.08 TW cm^{-2} intensity) within the Nanoscribe Photonic Professional GT+ system. This laser exposure occurred through a 63× oil immersion objective, Zeiss (with a numerical aperture of 1.4), using a "Galvo" configuration where galvanometric mirrors scan the laser beam laterally while vertical movement is controlled by piezo actuators. The specific parameters used for printing the nanopillar structures were 75% laser power and a scanning speed of 50 mm s^{-1}. The slicing distance (between adjacent layers) and hatching distance (between adjacent lines) parameters were set to 0.3 and 0.1 μm, respectively.

Sample Preparation for Cell Culture: Sterile 13 mm glass fused silica coverslips with nanopillars were left in 70% ethanol in H_2O to sterilize them. After 3× wash with phosphate-buffered saline (PBS), the samples were placed in a 24 well-plate and were coated using poly-L-Lysine solution (Sigma) for 2 h at room temperature, protected from light. Samples were then washed 3× in sterile Milli-Q and dried in the incubator at 37 °C before use. The three cell types employed in this study involved one primary neuronal model and two stem-cell-derived neuronal models: i) mouse primary hippocampal neurons, ii) human NPCs, and iii) human induced pluripotent stem-cell-derived I^3Neurons.

Primary Hippocampal Neurons: Primary hippocampal neuronal cultures were prepared from surplus brain tissue from FvB wild-type mice euthanized for other experiments (national authority Centrale Commisie Dierproeven, approval number AVD1010020197365). The cultures were prepared according to the procedure described by Banker and Goslin.[63] Brains, minus the cerebellum, from P1 pups were collected and transported in HBSS (Hanks' Balanced Salt Solution, Gibco) on ice. Hippocampi were isolated and collected altogether in a 10 mL tube containing 10 mL neurobasal (NB) medium (Gibco) on ice. Samples were washed twice in cold NB and incubated in prewarmed trypsin/EDTA solution (Gibco) for 20–30 min at 37 °C. Following incubation, hippocampi were washed twice in prewarmed NB and dissociated in NB supplemented with 2% B27 with vitamin A, 1% GlutaMAX, and 1% penicillin/streptomycin (P/S, all Gibco). After dissociation, cells were counted, and 10 000 cells/well were seeded in a 20 μL drop directly on top of the nanopillars. The cells were placed in the incubator for 45 min to 1 h to allow the cells to adhere to the nanopillars. Afterward, a supplemented medium was added to each well. Plates were stored in an incubator at 37 °C, and 5% CO_2, and half of the volume of the medium was refreshed every 7 days. Hippocampal neurons were cultured directly on the nanopillar arrays for 14 DIV before fixation.

Neural Progenitor Cells: Neuronal cultures were derived from NPCs, predifferentiated from human induced pluripotent stem cells (WTC-11 iPSCs), with passages 3.4–3.6 as described earlier by Gunhanlar et al.[64] After passage 3, NPC cultures were purified using fluorescence-activated cell sorting (FACS) as described previously.[65] Briefly, NPCs were detached from the culture plate and resuspended into a single-cell solution. $CD184^+/CD44^-/CD271^-/CD24^+$ cells were collected using an FACSAria III (BD Bioscience) and expanded in NPC medium. NPCs were used for experiments between passages 3 and 7 after sorting or differentiated to neural networks. A 10 cm dish was coated with 20 μg mL^{-1} laminin (Sigma) for at least 20 min at 37 °C. NPCs were taken from liquid nitrogen, thawed, and plated on the laminin coating in NPC medium (Advanced DMEM/F12, 1% N_2 supplement, 2% B27 supplement, 1% P/S, 1 μg mL^{-1} laminin, and 20 μg mL^{-1} basic fibroblast growth factor (Sigma)). The medium was refreshed three times a week, and cells were passaged and plated for neuronal differentiation when 80% confluency was reached (i.e., after 2–5 days). Once the plate was 80% full, cells were washed with Dulbecco's phosphate-buffered saline, incubated with accutase (Sigma), and dissociated in neural differentiation medium (specific for cortical neurons). Neural differentiation medium consists of neurobasal medium supplemented with 1% N_2 supplement, 2% B27 supplement without vitamin A, 1% P/S, 1% MEM (Minimum Essential Medium) nonessential amino acid solution (all Gibco), 2 μg mL^{-1} laminin (Sigma), 20 ng mL^{-1} brain-derived neurotrophic factor, 20 ng mL^{-1} glial-cell-derived neurotrophic factor (both Bio-connect), 1 μM dibutyryl cyclic adenosine monophosphate, and 200 μM ascorbic acid (both Sigma). In each well, a 20 μL drop with 10 000 or 50 000 cells was placed directly on top of the nanopillars for 1 h to allow the cells to attach. After 1 h, 750 μL of neural differentiation medium was added to each well. Cells were kept in an incubator at 37 °C and 5% CO_2. The medium was refreshed three times per week. During weeks 1–4, the medium was fully refreshed. After 4 weeks, only half of the volume of the medium was refreshed. WtC-11 and I^3N cells (also derived from WTC-11) were obtained from Gladstone institute under MTA. WTC-11 cells are human induced pluripotent stem cells registered in hPSCreg under UCSFi001-A, with evidence of ethical provenance provided. As such, both types of samples are publicly available and not derived from human tissue acquired during the project, and no ethical approval is necessary.

I^3Neurons: Human iPSC-derived glutamatergic cortical neurons were generated as previously described, through the induced differentiation of i^3N human iPSCs.[48] i^3N iPSCs harbor a neurogenin-2 transgene under a tetracycline-inducible promoter stably integrated into the AAVS1 genomic safe harbor locus, which allows for rapid inducible differentiation to cortical neurons.[48,66] i^3N iPSCs were cultured as described previously[67] but with some minor modifications, as indicated in the following sections. i^3N iPSCs were cultured on Geltrex (Thermo Scientific) coated 6-well plates in 2 mL Gibco StemFlex medium (Thermo Scientific), which was replaced every 2 days for ≈5 days until the wells reached ≈70% confluency, after which the cells were replated. Replating was done by aspirating the culture medium, washing once with PBS, followed by gentle detachment by incubation with 1 mL EDTA (0.5 mM) for 5 min at 37 °C, 5% CO_2. Detached cell clusters were then reseeded in 2 mL Stemflex medium in a fresh Geltrex-coated well. To generate I^3 Neurons, i^3N iPSCs were predifferentiated and differentiated as described previously.[67] Briefly, iPSCs were dissociated by incubating with 1 mL acutase (StemCell Technologies) for 5 min, and re-plated as single cells in neuronal induction medium containing doxycycline (IM). IM was replaced every day. After 3 days of predifferentiation, 100 000 cells were frozen in Bambanker at −80 °C overnight in a cryobox, and subsequently stored in liquid nitrogen. To induce neuronal differentiation, cells were thawed and directly plated (10 000 cells/well) onto the nanopatterned substrates (sterilized and coated as before) in neuronal differentiation medium. To maintain these cultures and allow further differentiation, half of the medium was changed every 3 to 4 days. Cells were kept in culture for 2 or 7 days and were then fixed for observation with the different methods described below. WtC-11 and I^3N cells (also derived from WTC-11) were obtained from Gladstone Institute under MTA. WTC-11 cells are human induced pluripotent stem cells registered in hPSCreg under UCSFi001-A, with evidence of ethical provenance being provided. As such both types of samples are publicly available and not derived from human tissue acquired during the project, and no ethical approval is necessary.

Scanning Electron Microscopy: To prepare the sample for SEM characterization, cells were rinsed 3× with PBS and incubated in 2.5% glutaraldehyde in water for 2 h at room temperature. The glutaraldehyde was then removed, and cells were rinsed 3× with PBS, followed by a secondary fixation with 1% osmium tetroxide (TCI Chemicals) in water for 1 h at room temperature in order to preserve cell morphology. After another PBS rinsing, samples were dehydrated using 30%, 50%, 70%, 85%, 90%, and 2 × 100% ethanol for 5 min each, and then immersed in 50%, 75%, and

100% solutions of hexamethyldisilazane (HMDS, Sigma–Aldrich) in 100% ethanol for 5 min each. Finally, the residual HMDS was allowed to evaporate overnight. The whole protocol was carried out under a chemical fume hood. Afterward, samples were coated with 50 nm of gold using a sputter coater JEOL JFC-1300 and imaged in high vacuum using a JEOL 6010LA scanning electron microscope at 10 kV voltage acceleration.

Mechanical Characterization: The mechanical characterization of the 3D-printed materials was performed on $30 \times 30 \times 30$ µm^3 cubes ($n = 5$), manufactured using the same printing parameters of the nanopillar arrays. An FT-NMT03 nanomechanical testing system (Femtotools) was then employed to compress the cubes using a silicon 50×50 µm^2 tip until 10% compression, and the Young's modulus of the material was extrapolated from the linear loading phase of the stress–strain curve (Figure S2, Supporting Information). The same approach was followed for the compression of the micropillar arrays ($n = 5$), including 10×10 pillars covering an overall surface area of 30×30 µm^2 for each nanopillar height (0.6, 1, 2.3, 3.3, and 5 µm).

Immunofluorescence Staining and Confocal Imaging Configuration: To perform immunofluorescence staining for confocal microscopy, cells were fixed with 4% paraformaldehyde in PBS for 15 min, permeabilized in 0.5% Triton X-100 in PBS for 10 min, and nonspecific protein binding sites were blocked with 2% bovine serum albumin (BSA) in PBS for 1 h at room temperature (RT). Depending on the experiment, samples were incubated with the primary antibodies in dilution buffer (0.5% BSA, Triton-X 0.1%/PBS): rabbit antibeta III tubulin (1:1000, Abcam, ab17208), mouse antivinculin (1:500, Abcam, ab130007), mouse antiSynapsin I a/b (A-8) (1:200, Santa Cruz biotech., sc-376623) 1 h at RT. Afterward, samples were washed twice with PBS, and secondary antibodies were used to detect the primary ones: goat anti-rabbit IgG H&L (Alexa Fluor 488) (1:1000, Abcam, ab150077), goat antimouse IgG H&L (Alexa Fluor 647) (1:1000, Abcam, ab150115) alongside with Alexa Fluor 647 phalloidin (1:1000, Invitrogen, A22287) or Alexa Fluor 568 phalloidin (1:1000, Invitrogen, A12380) staining to visualize the F-Actin for 60 min at room temperature. The nuclei were stained with either Hoechst 33258 (1:2000 dilution, Molecular Probes) for 10 min or by mounting the samples in ProLong Gold Antifade Mountant with DNA stain DAPI (Thermo Fisher) and stored for long-term observation. After the staining, in case of Hoechst, cells were immersed and stored in PBS and kept in 4 °C. Confocal imaging experiments were performed using a Dragonfly 200 upright spinning disk confocal microscope (Andor). Four excitation laser wavelengths were employed to excite the fluorophores (405, 488, 561, and 640 nm) and four bandpass filter corresponding the excitation lasers above to filter the emission of the samples (445 ± 46, 521 ± 38, 594 ± 43, and 685 ± 47 nm). For large-area acquisitions of whole nanopillar strips, a water dipping 25× apochromat lens (NA = 1.19, Nikon) was used (samples were immersed in PBS for the whole acquisition time), whereas for high-resolution images of individual growth cones, an oil immersion 60× TIRF apochromat lens (NA = 1.49, Nikon) was employed with a cover glass on top of the samples. The samples were acquired using *z*-stacks and Montage mode in the fusion software (Andor), and the maximum intensity *Z* projections, 3D reconstructions, and 2D image visualization were performed using Imaris 2.1 software (Oxford Instruments).

STORM Imaging Buffer and Super-Resolution Imaging Setup: The refractive-index-matched buffer was prepared according to the protocol by Lee et al.[61] and consisted of 100 mM cysteamine (30070, Sigma–Aldrich), 10% (w/v) glucose (G7021, Sigma–Aldrich), 0.8 mg mL^{-1} glucose oxidase (G2133, Sigma–Aldrich), 40 µg mL^{-1} catalase (C40, Sigma–Aldrich), and 82% (v/v) 3-pyridinemethanol (A10381, Thermo Fisher Scientific) in PBS. Imaging buffer was made fresh every time using stocks: 1 M cysteamine (pH 8.0 using HCl), 50% glucose, 80 mg mL^{-1} glucose oxidase, and 4 mg mL^{-1} catalase, all in PBS. Enzymes and cysteamine stocks were kept at 4 °C for no more than 2 weeks. For each acquisition, 20 000 frames were recorded using the same Andor confocal above, operating with a 488 nm laser at 60–100% laser power (maximum power 791 mW before the objective) and a 640 nm laser (maximum power 255 mW before the objective) at 70–100% laser power. The fluorophores were activated by briefly irradiating the sample with a 405 nm laser at 20% laser power every ≈5000 frames. After imaging, all frames were inserted in Picasso software,[68] where the spots were localized according to the set threshold, and the final image was reconstructed by combining those localizations. An oil immersion 60× TIRF apochromat lens (NA = 1.49, Nikon) was employed with a cover glass on top of the samples (for additional information, see Figure S6 in the Supporting Information).

Directionality Analysis: Confocal images of all three different cell lines were used to calculate the directionality of the neuritic processes. β-tubulin III channel confocal images were analyzed in ImageJ software[69] and the directionality of each array was calculated by using the OrientationJ plugin[70] (Figure S3, Supporting Information). The data were exported as degree values from −90° up to +90° divided into subsections of 0.5°. Then the values were plotted normalized to the highest measurement value of each array. Plots were reported as the average value of three independent experiments.

Neurite Length Analysis: Confocal images of I^{3}Neurons were used to evaluate the neurite lengths. First, the cyan channel (nuclei) was recorded, and then the green channel (β-tubulin III). Then, both channels were inserted in CellProfiler,[71] where a custom-made pipeline was used. In brief, both channels turned in 8-bit grayscale images, and the nuclei were masked using the identify primary object module. Then, the green channel containing the tubulin was thresholded, masked, and skeletonized. Finally, the nuclei were used as a seeding structure to calculate the image skeleton through the module measure object skeleton; the data were exported into a spreadsheet and inserted into GraphPad Prism for further analysis.

Statistical Analysis: The data were analyzed using GraphPad Prism 9.5.1. A one-way analysis of variance (ANOVA) test was used to determine the statistical significance. Tukey multiple comparisons test was performed for comparing the multiple data sets. The *p*-values related to the statistical significance and the sample size (*n*) for each test are displayed in the related figure captions. For directionality analysis, ImageJ was used with the orientationJ plugin, and then data were imported into Excel, where the average of each orientation was calculated with the standard deviation.

Supporting Information

Supporting Information is available from the Wiley Online Library or from the author.

Acknowledgements

The authors acknowledge the technical support of the PME Lab and the Nanoscribe team from Delft University of Technology for the provided help related to two-photon polymerization optimization. The authors acknowledge Bruce R. Conklin for providing the parental WTC-11 cells (The Gladstone Institute, UCSF), Li Gan (The Gladstone institute) for providing the I^{3}N cells and acknowledge the help of the Erasmus MC iPS core facility. The authors also acknowledge Hei-Ling Lu and Martijn Schonewille at Erasmus MC for donation of mouse hippocampal cells. A.A. acknowledges support by the Dutch Research Council (Nederlandse Organisatie voor Wetenschappelijk Onderzoek) grant number OCENW.XS22.1.021 and the TU Delft Mechanical Engineering Cohesion grants program. In addition, H.S. and F.M.S.d.V. were supported by the Erasmus MC Human Disease Model Award. D.B. acknowledges support by an NWO Start-up Grant (Grant No. 740.018.018) and ERC Starting Grant (Grant No. 850818 – MULTIVIsion). Mouse Hippocampal neurons were obtained as part of study plans SP2200257 and SP2300159, under National Ethical Approval License (CCD) AVD1010020197365. The WTC-11 iPSC line was provided by Bruce R. Conklin and the I^{3}N cells by Li Gan (The Gladstone Institutes and UCSF).

Conflict of Interest

The authors declare no conflict of interest.

Data Availability Statement

The data that support the findings of this study are available from the corresponding author upon reasonable request.

Keywords

effective shear modulus, growth cone, neuro-mechanobiology, neurons, two-photon polymerization

Received: May 31, 2024
Revised: September 30, 2024
Published online:

---

[1] L. Castillo Ransanz, P. F. J. Van Altena, V. M. Heine, A. Accardo, *Front. Bioeng. Biotechnol.* **2022**, *10*, 1096054.
[2] L. A. Lowery, D. Van Vactor, *Nat. Rev. Mol. Cell Biol.* **2009**, *10*, 332.
[3] E. Tamariz, A. Varela-Echavarría, *Front. Neuroanat.* **2015**, *9*, 91599.
[4] M. Z. Chauhan, J. Arcuri, K. K. Park, M. K. Zafar, R. Fatmi, A. S. Hackam, Y. Yin, L. Benowitz, J. L. Goldberg, M. Samarah, S. K. Bhattacharya, *iScience* **2020**, *23*, 100836.
[5] P. C. Kerstein, R. H. Nichol, T. M. Gomez, *Front. Cell. Neurosci.* **2015**, *9*, 151038.
[6] R. S. Fischer, P. Y. Lam, A. Huttenlocher, C. M. Waterman, *Dev. Biol.* **2019**, *451*, 86.
[7] J. P. Myers, T. M. Gomez, *J. Neurosci.* **2011**, *31*, 13585.
[8] M. Burute, K. I. Jansen, M. Mihajlovic, T. Vermonden, L. C. Kapitein, *Sci. Adv.* **2022**, *8*, 2343.
[9] F. Sala, C. Ficorella, R. Martínez Vázquez, H. M. Eichholz, J. A. Käs, R. Osellame, *Front. Bioeng. Biotechnol.* **2021**, *9*, 664094.
[10] T. E. Santos, B. Schaffran, N. Broguière, L. Meyn, M. Zenobi-Wong, F. Bradke, *Cell Rep.* **2020**, *32*, 107907.
[11] E. A. Aisenbrey, W. L. Murphy, *Nat. Rev. Mater.* **2020**, *5*, 539.
[12] M. C. Mosley, H. J. Lim, J. Chen, Y. H. Yang, S. Li, Y. Liu, L. A. Smith Callahan, *J. Biomed. Mater. Res., Part A* **2017**, *105*, 824.
[13] A. K. Rajendran, D. Sankar, S. Amirthalingam, H. D. Kim, J. Rangasamy, N. S. Hwang, *Biomater. Res.* **2023**, *27*, 55.
[14] C. Simitzi, A. Ranella, E. Stratakis, *Acta Biomater.* **2017**, *51*, 21.
[15] N. Marinval, S. Y. Chew, *APL Bioeng.* **2021**, *5*, 021505.
[16] K. J. Lampe, A. L. Antaris, S. C. Heilshorn, *Acta Biomater.* **2013**, *9*, 5590.
[17] S. M. de Leeuw, S. Davaz, D. Wanner, V. Milleret, M. Ehrbar, A. Gietl, C. Tackenberg, *J. Neurosci. Methods* **2021**, *360*, 109254.
[18] U. A. Aregueta-Robles, P. J. Martens, L. A. Poole-Warren, R. A. Green, *Acta Biomater.* **2019**, *95*, 269.
[19] S. Fan, L. Qi, J. Li, D. Pan, Y. Zhang, R. Li, C. Zhang, D. Wu, P. Lau, Y. Hu, G. Bi, W. Ding, J. Chu, S. Fan, W. Ding, L. Qi, P. Lau, G. Bi, J. Li, D. Pan, Y. Zhang, R. Li, C. Zhang, D. Wu, Y. Hu, J. Chu, *Adv. Healthcare Mater.* **2021**, *10*, 2100094.
[20] A. Solanki, S. T. D. Chueng, P. T. Yin, R. Kappera, M. Chhowalla, K. B. Lee, *Adv. Mater.* **2013**, *25*, 5477.
[21] G. S. Lorite, L. Ylä-Outinen, L. Janssen, O. Pitkänen, T. Joki, J. T. Koivisto, M. Kellomäki, R. Vajtai, S. Narkilahti, K. Kordas, *Nano Res.* **2019**, *12*, 2894.
[22] A. Cutarelli, S. Ghio, J. Zasso, A. Speccher, G. Scarduelli, M. Roccuzzo, M. Crivellari, N. M. Pugno, S. Casarosa, M. Boscardin, L. Conti, *Cells* **2020**, *9*, 88.
[23] C. H. Rasmussen, P. M. Reynolds, D. R. Petersen, M. Hansson, R. M. McMeeking, M. Dufva, N. Gadegaard, *Adv. Funct. Mater.* **2016**, *26*, 815.
[24] A. Sharaf, B. Roos, R. Timmerman, G. J. Kremers, J. J. Bajramovic, A. Accardo, *Front. Bioeng. Biotechnol.* **2022**, *10*, 926642.
[25] A. Sharaf, R. Timmerman, J. Bajramovic, A. Accardo, *Neural Regener. Res.* **2022**, *18*, 1709.
[26] C. Conci, E. Jacchetti, L. Sironi, L. Gentili, G. Cerullo, R. Osellame, G. Chirico, M. T. Raimondi, *Adv. Opt. Mater.* **2022**, *10*, 2101103.
[27] G. Flamourakis, I. Spanos, Z. Vangelatos, P. Manganas, L. Papadimitriou, C. Grigoropoulos, A. Ranella, M. Farsari, *Macromol. Mater. Eng.* **2020**, *305*, 2070016.
[28] E. Yarali, A. A. Zadpoor, U. Staufer, A. Accardo, M. J. Mirzaali, *ACS Appl. Bio Mater.* **2023**, *6*, 2562.
[29] Q. Akolawala, F. Keuning, M. Rovituso, W. van Burik, E. van der Wal, H. H. Versteeg, A. M. R. Rondon, A. Accardo, *Adv. Healthcare Mater.* **2024**, *13*, 2302988.
[30] Q. Akolawala, M. Rovituso, H. H. Versteeg, A. M. R. Rondon, A. Accardo, *ACS Appl. Mater. Interfaces* **2022**, *14*, 20778.
[31] N. Barin, H. E. Balcioglu, I. de Heer, M. de Wit, M. L. M. Lamfers, M. E. van Royen, P. J. French, A. Accardo, *Small* **2022**, *18*, 2204485.
[32] E. Yarali, M. Klimopoulou, K. David, P. E. Boukany, U. Staufer, L. E. Fratila-Apachitei, A. A. Zadpoor, A. Accardo, M. J. Mirzaali, *Acta Biomater.* **2024**, *177*, 228.
[33] E. D. Lemma, B. Spagnolo, M. De Vittorio, F. Pisanello, *Trends Biotechnol.* **2019**, *37*, 358.
[34] E. D. Lemma, F. Rizzi, T. Dattoma, B. Spagnolo, L. Sileo, A. Qualtieri, M. De Vittorio, F. Pisanello, *IEEE Trans. Nanotechnol.* **2017**, *16*, 23.
[35] L. Pertoldi, V. Zega, C. Comi, R. Osellame, *J. Appl. Phys.* **2020**, *128*, 175102.
[36] P. F. J. van Altena, A. Accardo, *Polymers* **2023**, *15*, 1816.
[37] T. Koch, W. Zhang, T. T. Tran, Y. Wang, A. Mikitisin, J. Puchhammer, J. R. Greer, A. Ovsianikov, F. Chalupa-Gantner, M. Lunzer, *Adv. Mater.* **2024**, *36*, 2308497.
[38] Y. Kim, S. M. Meade, K. Chen, H. Feng, J. Rayyan, A. Hess-Dunning, E. S. Ereifej, *Front. Neurosci.* **2018**, *12*, 387780.
[39] A. Jacinto, L. Wolpert, *Curr. Biol.* **2001**, *11*, R634.
[40] A. R. Costa, R. Pinto-Costa, S. C. Sousa, M. M. Sousa, *Front. Mol. Neurosci.* **2018**, *11*, 396729.
[41] A. I. Son, J. D. Opfermann, C. McCue, J. Ziobro, J. H. Abrahams, K. Jones, P. D. Morton, S. Ishii, C. Oluigbo, A. Krieger, J. S. Liu, K. Hashimoto-Torii, M. Torii, *Sci. Rep.* **2017**, *7*, 17624.
[42] A. Sharaf, J. P. Frimat, G. J. Kremers, A. Accardo, *Micro Nano Eng.* **2023**, *19*, 100188.
[43] L. Agrawal, M. Saidani, L. Guillaud, M. Terenzio, *Mater. Sci. Eng., C* **2021**, *131*, 112502.
[44] S. Schweiger, T. Schulze, S. Schlipf, P. Reinig, H. Schenk, *J. Opt. Microsyst.* **2022**, *2*, 033501.
[45] J. Purtov, A. Verch, P. Rogin, R. Hensel, *Microelectron. Eng.* **2018**, *194*, 45.
[46] F. Falleroni, U. Bocchero, S. Mortal, Y. Li, Z. Ye, D. Cojoc, V. Torre, *iScience* **2022**, *25*, 103807.
[47] Y. Zhang, C. H. Pak, Y. Han, H. Ahlenius, Z. Zhang, S. Chanda, S. Marro, C. Patzke, C. Acuna, J. Covy, W. Xu, N. Yang, T. Danko, L. Chen, M. Wernig, T. C. Südhof, *Neuron* **2013**, *78*, 785.
[48] C. Wang, M. E. Ward, R. Chen, K. Liu, T. E. Tracy, X. Chen, M. Xie, P. D. Sohn, C. Ludwig, A. Meyer-Franke, C. M. Karch, S. Ding, L. Gan, *Stem Cell Rep.* **2017**, *9*, 1221.
[49] F. Chen, P. W. Tillberg, E. S. Boyden, *Science* **2015**, *347*, 543.
[50] A. Zink, P. Lisowski, A. Prigione, *Bio. Protoc.* **2021**, *11*, e3939.
[51] F. H. Nazir, B. Becker, A. Brinkmalm, K. Höglund, Å. Sandelius, P. Bergström, T. M. Satir, A. Öhrfelt, K. Blennow, L. Agholme, H. Zetterberg, *Neurochem. Int.* **2018**, *121*, 38.
[52] F. Milos, A. Belu, D. Mayer, V. Maybeck, A. Offenhäusser, *Adv. Biol.* **2021**, *5*, 2000248.

[53] S. Kang, X. Chen, S. Gong, P. Yu, S. Yau, Z. Su, L. Zhou, J. Yu, G. Pan, L. Shi, *Sci. Rep.* **2017**, *7*, 12233.
[54] C. A. Short, E. A. Suarez-Zayas, T. M. Gomez, *Curr. Opin. Neurobiol.* **2016**, *39*, 77.
[55] J. D. Jontes, J. A. Buchanan, S. J. Smith, *Nat. Neurosci.* **2000**, *3*, 231.
[56] A. Herrera, J. Hellwig, H. Leemhuis, R. von Klitzing, I. Heschel, G. N. Duda, A. Petersen, *Mater. Sci. Eng., C* **2019**, *103*, 109760.
[57] J. J. Licari, D. W. Swanson, in *Adhesives Technology for Electronic Applications: Materials, Processing, Realiability*, William Andrew, Waltham, MA **2011**, pp. 345–377.
[58] E. Alfadil, F. Bradke, *Semin. Cell Dev. Biol.* **2023**, *140*, 63.
[59] W. H. Goldmann, *Cell Biol. Int.* **2016**, *40*, 241.
[60] D. Y. Wang, C. Melero, A. Albaraky, P. Atherton, K. A. Jansen, A. Dimitracopoulos, F. Dajas-Bailador, A. Reid, K. Franze, C. Ballestrem, *Exp. Cell Res.* **2021**, *407*, 112805.
[61] Y. Lee, Y. Lee, M. Lee, D. Koo, D. Kim, H. Kim, K. Lee, J. Kim, *ACS Photonics* **2023**, *10*, 2589.
[62] A. Shapson-Coe, M. Januszewski, D. R. Berger, A. Pope, Y. Wu, T. Blakely, R. L. Schalek, P. H. Li, S. Wang, J. Maitin-Shepard, N. Karlupia, S. Dorkenwald, E. Sjostedt, L. Leavitt, D. Lee, J. Troidl, F. Collman, L. Bailey, A. Fitzmaurice, R. Kar, B. Field, H. Wu, J. Wagner-Carena, D. Aley, J. Lau, Z. Lin, D. Wei, H. Pfister, A. Peleg, V. Jain, et al., *Science* **2024**, *384*, eadk4858.
[63] G. Banker, K. Goslin, in *Culturing Nerve Cells*, MIT Press, Cambridge, MA **1991**, p. 453.
[64] N. Gunhanlar, G. Shpak, M. van der Kroeg, L. A. Gouty-Colomer, S. T. Munshi, B. Lendemeijer, M. Ghazvini, C. Dupont, W. J. G. Hoogendijk, J. Gribnau, F. M. S. de Vrij, S. A. Kushner, *Mol. Psychiatry* **2017**, *23*, 1336.
[65] S. H. Yuan, J. Martin, J. Elia, J. Flippin, R. I. Paramban, M. P. Hefferan, J. G. Vidal, Y. Mu, R. L. Killian, M. A. Israel, N. Emre, S. Marsala, M. Marsala, F. H. Gage, L. S. B. Goldstein, C. T. Carson, *PLoS One* **2011**, *6*, 17540.
[66] M. S. Fernandopulle, R. Prestil, C. Grunseich, C. Wang, L. Gan, M. E. Ward, *Curr. Protoc. Cell Biol.* **2018**, *79*, e51.
[67] A. Dema, R. Charafeddine, S. Rahgozar, J. van Haren, T. Wittmann, *Elife* **2023**, *12*, 84143.
[68] M. T. Strauss, *Commun. Biol.* **2022**, *5*, 930.
[69] C. A. Schneider, W. S. Rasband, K. W. Eliceiri, *Nat. Methods* **2012**, *9*, 671.
[70] Z. Püspöki, M. Storath, D. Sage, M. Unser, *Adv. Anat., Embryol. Cell Biol.* **2016**, *219*, 69.
[71] D. R. Stirling, M. J. Swain-Bowden, A. M. Lucas, A. E. Carpenter, B. A. Cimini, A. Goodman, *BMC Bioinform.* **2021**, *22*, 433.